# Efficient Cell-Vertex Multigrid Scheme for the Three-Dimensional Navier-Stokes Equations

R. Radespiel* and C. Rossow†
*Institute for Design Aerodynamics, Federal Republic of Germany*
and
R. C. Swanson‡
*NASA Langley Research Center, Hampton, Virginia 23665*

**A cell-vertex scheme for the three-dimensional Navier–Stokes equations, which is based on central-difference approximations and Runge–Kutta time stepping, is described. By using local time stepping, implicit residual smoothing with locally varying coefficients, a multigrid method, and carefully controlled dissipative terms, very good convergence rates are obtained for two- and three-dimensional flows. Details of the acceleration techniques, which are important for convergence on meshes with high-aspect-ratio cells, are discussed. Emphasis is placed on the analysis of the implicit smoothing of the explicit residuals with coefficients, which depend on cell aspect ratios.**

## Introduction

In recent years, considerable advancement has been achieved in the numerical solution of the Euler and Navier–Stokes equations. Nevertheless, existing computer codes for the solution of the three-dimensional Navier–Stokes equations require large computing times. In order to make Navier–Stokes solutions useful in the flight vehicle design process, substantial improvements in the efficiency and accuracy of the algorithms have to be made.

Finite-volume methods based on explicit Runge–Kutta time-stepping schemes have been shown to be very efficient in the solution of the Euler equations governing inviscid flows.[1,2] They are in widespread use now. More recently, they have been extended for a solution of the mass-averaged Navier–Stokes equations. The convergence of the basic scheme to the desired steady-state solution, however, slows down considerably because of the time-step limitation associated with the small mesh cells that are necessary to resolve the thin shear layers. This drawback of the explicit scheme can be overcome by applying several acceleration techniques, namely, local time stepping, implicit residual averaging, and a multigrid algorithm. Successful applications of these techniques have been reported in Refs. 3 and 4 for two-dimensional flow, and there has been partial success in three dimensions also.[5]

In the present work, a recently developed efficient and robust finite-volume multigrid scheme for the three-dimensional Navier–Stokes equations is presented. This method is an extension of a code for the Euler equations as described in Ref. 6. A cell-vertex discretization is employed rather than the usual cell-centered discretization because an analysis of the discretization errors indicates lower errors for meshes with high stretching or discontinuities in slope. As the scheme is based on central differencing, an artificial viscosity model is used, which is specially designed for high-aspect-ratio cells. Also, the boundary treatment of the dissipative terms, which is important for an accurate prediction of the skin friction, is discussed. A multistage Runge–Kutta time-stepping algorithm is used to advance the solution in time. The acceleration techniques, which are applied to obtain faster convergence, are discussed in detail. In particular, the implicit smoothing of the explicit residuals has been tailored to high-aspect-ratio cells and will be analyzed. Also, some special procedures for enhancing the performance of the multigrid method are described. Numerical results for transonic flows around the ONERA-M6 wing are given. Good convergence behavior is obtained on a dense coordinate mesh of $289 \times 65 \times 49$ points. It is shown that convergence to engineering accuracy is obtained within less than 100 multigrid cycles.

## Governing Equations

The integral form of the mass-averaged Navier–Stokes equations using nondimensional variables can be written as

$$\frac{\partial}{\partial t}\iiint_V W \, dV + \iint_{\partial V} \bar{F}\boldsymbol{n} \, dS = 0 \tag{1}$$

where

$$W = (\rho \; \rho u \; \rho v \; \rho w \; \rho E)^T$$

is the vector of conserved quantities with $\rho$, $u$, $v$, $w$, and $E$ denoting the density, the Cartesian velocity components, and the specific total integral energy. The quantity $V$ denotes an arbitrary control volume with the boundary $\partial V$ and the outer normal $\boldsymbol{n}$. The flux density tensor $\bar{F}$ may be divided into its convective part $\bar{F}_c$ and its viscous part $\bar{F}_v$ as

$$\bar{F} = \bar{F}_c - \bar{F}_v$$

$$\bar{F}_c = \begin{bmatrix} \rho u \boldsymbol{i}_x + \rho v \boldsymbol{i}_y + \rho w \boldsymbol{i}_z \\ (\rho u^2 + p)\boldsymbol{i}_x + \rho u w \boldsymbol{i}_y + \rho u w \boldsymbol{i}_z \\ \rho u v \boldsymbol{i}_x + (\rho v^2 + p)\boldsymbol{i}_y + \rho v w \boldsymbol{i}_z \\ \rho u w \boldsymbol{i}_x + \rho v w \boldsymbol{i}_y + (\rho w^2 + p)\boldsymbol{i}_z \\ (\rho u E + u p)\boldsymbol{i}_x + (\rho v E + v p)\boldsymbol{i}_y + (\rho w E + w p)\boldsymbol{i}_z \end{bmatrix}$$

$$\bar{F}_v = \begin{bmatrix} 0 \\ \sigma_{xx}\boldsymbol{i}_x + \sigma_{xy}\boldsymbol{i}_y + \sigma_{xz}\boldsymbol{i}_z \\ \sigma_{yx}\boldsymbol{i}_x + \sigma_{yy}\boldsymbol{i}_y + \sigma_{yz}\boldsymbol{i}_z \\ \sigma_{zx}\boldsymbol{i}_x + \sigma_{zy}\boldsymbol{i}_y + \sigma_{zz}\boldsymbol{i}_z \\ \Pi_x \boldsymbol{i}_x + \Pi_y \boldsymbol{i}_y + \Pi_z \boldsymbol{i}_z \end{bmatrix}$$

Received April 26, 1989; revision received Oct. 23, 1989. 

*Research scientist, Aerothermodynamics section.
†Research scientist, Propulsion Integration section.
‡Research scientist, Theoretical Flow Physics branch, Fluid Mechanics division. Member AIAA.

with

$$\Pi_x = (u\sigma_{xx} + v\sigma_{xy} + w\sigma_{xz} - q_x)\boldsymbol{i}_x$$

$$\Pi_y = (u\sigma_{yx} + v\sigma_{yy} + w\sigma_{yz} - q_y)\boldsymbol{i}_y$$

$$\Pi_z = (u\sigma_{zx} + v\sigma_{zy} + w\sigma_{zz} - q_z)\boldsymbol{i}_z$$

The equation of state for an ideal gas is used to calculate the pressure and temperature. That is,

$$p = (\gamma - 1)\rho\left[E - \frac{(u^2+v^2)}{2}\right] \tag{2a}$$

$$T = \frac{p}{\rho} \tag{2b}$$

The elements of the shear-stress tensor and heat-flux vector are given by the constitutive equations for a Newtonian fluid as follows:

$$\begin{aligned}
\sigma_{xx} &= 2\mu u_x - \frac{2}{3}\mu(u_x + v_y + w_z)\\
\sigma_{yy} &= 2\mu v_y - \frac{2}{3}\mu(u_x + v_y + w_z)\\
\sigma_{zz} &= 2\mu v_z - \frac{2}{3}\mu(u_x + v_y + w_z)\\
\sigma_{xy} &= \sigma_{yx} = \mu(u_y + v_x)\\
\sigma_{xz} &= \sigma_{zx} = \mu(u_z + w_x)\\
\sigma_{yz} &= \sigma_{zy} = \mu(v_z + w_y)
\end{aligned} \tag{3}$$

$$q_x = -k\frac{\partial T}{\partial x}, \qquad q_y = -k\frac{\partial T}{\partial y}, \qquad q_z = -k\frac{\partial T}{\partial z}$$

The nondimensional viscosity $\mu$ is assumed to follow an empirical power law

$$\mu = \frac{\gamma^{1/2}M_\infty}{Re_\infty}\left(\frac{T}{T_\infty}\right)^{0.75} \tag{4}$$

and the heat conductivity is

$$k = \frac{\gamma}{\gamma - 1}\frac{\mu}{Pr} \tag{5}$$

For turbulent flows, the laminar viscosity $\mu$ is replaced by $\mu + \mu_t$, and $\mu/Pr$ is replaced by $\mu/Pr + \mu_t/Pr_t$, where the eddy viscosity $\mu_t$ and the turbulent Prandtl number $Pr_t$ are provided by a turbulence model. In the present work, the turbulence model of Baldwin and Lomax[7] and a nonequilibrium model, which is a modification of the work of Johnson and King,[8] are used.

## Spatial Discretization

The discretization of (1) follows the method of lines, i.e., discretization in space and time is done separately. The domain around the aerodynamic body is partitioned with hexahedrons. The discrete values of the flow quantitites are located at the vertices of the mesh cells. The integral equation (1) is approximated by the spatial discretization, yielding

$$\frac{\mathrm{d}}{\mathrm{d}t}\boldsymbol{W}_{i,j,k} = \frac{1}{V_{i,j,k}}(\boldsymbol{Q}_{c\,i,j,k} + \boldsymbol{Q}_{v\,i,j,k} + \boldsymbol{D}_{i,j,k}) \tag{6}$$

In the following, the net inflow of mass, momentum, and energy associated with the convective terms $\boldsymbol{Q}_{c\,i,j,k}$, the viscous terms $\boldsymbol{Q}_{v\,i,j,k}$, and the artificial dissipative terms $\boldsymbol{D}_{i,j,k}$ are discussed.

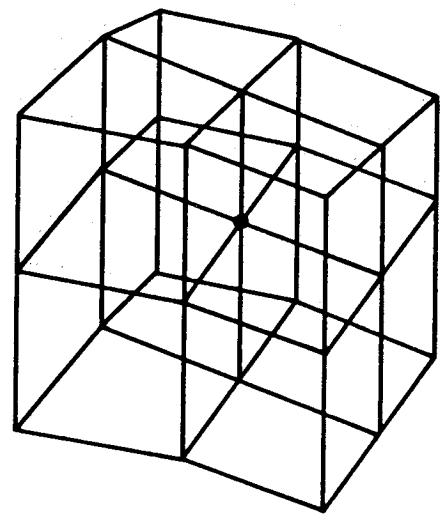

Fig. 1 Control volume around point $(i,j,k)$.

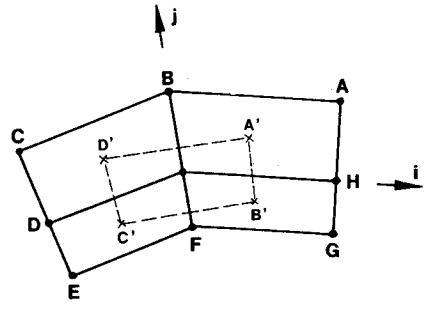


Fig. 2 Control volume in a plane grid.

Following Ref. 9, the discretization of the convective part of the flux density tensor is outlined. In the three-dimensional case, the eight cells surrounding a vertex form a super cell as shown in Fig. 1. To simplify the discussion, a plane mesh is shown in Fig. 2 where the super cell around a vertex $(i,j,k)$ is given by the points $A$, $B$, $C$, $D$, $E$, $F$, $G$, and $H$.

The surface integral of (1) over the convective part of the flux density tensor is evaluated for each component cell using an arithmetic average of the flux quantitites at the vertices to determine the values on each of the cell faces. Then, the resultant convective inflow of mass, momentum, and energy associated with point $(i,j,k)$ is computed by summing the contributions of the component cells. It can be shown[10] that this discretization is first-order accurate if the normal vector over each surface segment is smooth and the shape of the segment approaches a parallelogram with grid refinement. On completely smooth meshes, the discretization is second-order accurate.

Next, the viscous fluxes required to determine the solution at the point $(i,j,k)$ are approximated using the auxiliary cell with the dashed boundary shown in Fig. 2. Note that the volume of the auxiliary cell is given by the volume of the super cell divided by a factor of 8. The viscous fluxes contain first derivatives of the flow variables, which are computed using a local transformation from Cartesian coordinates to the curvilinear coordinates $\xi$, $\eta$, and $\zeta$, i.e.,

$$\phi_x = \frac{\partial\phi}{\partial\xi}\frac{\partial\xi}{\partial x} + \frac{\partial\phi}{\partial\eta}\frac{\partial\eta}{\partial x} + \frac{\partial\phi}{\partial\zeta}\frac{\partial\zeta}{\partial x} \tag{7}$$

The derivatives $\phi_\xi$, $\phi_\eta$, and $\phi_\zeta$ are approximated using finite differences, whereas the cell face vectors $\boldsymbol{S}_\xi$, $\boldsymbol{S}_\eta$, and $\boldsymbol{S}_\zeta$, which

are written as

$$\boldsymbol{S}_\xi = (S_{\xi x} S_{\xi y} S_{\xi z})^T$$

$$\boldsymbol{S}_\eta = (S_{\eta x} S_{\eta y} S_{\eta z})^T$$

$$\boldsymbol{S}_\zeta = (S_{\zeta x} S_{\zeta y} S_{\zeta z})^T$$

and the volume $V$ are used to compute metric derivatives. If $\phi_x$ is to be approximated at $(i+1/2,j,k)$, we obtain

$$(\phi_x)_{i+1/2,j,k} = \frac{(\delta_\xi \phi_{i+1/2,j,k} S_{\xi x_{i+1/2,j,k}} + \delta_\eta \phi_{i+1/2,j,k} S_{\eta x_{i+1/2,j,k}} + \delta_\zeta \phi_{i+1/2,j,k} S_{\zeta x_{i+1/2,j,k}})}{V_{i+1/2,j,k}} \tag{8}$$

where $\delta_\xi$, $\delta_\eta$, and $\delta_\zeta$ denote central-difference operators in the curvilinear coordinate directions. In practice, coordinate grids for the resolution of viscous shear layers are highly stretched in the direction normal to the layer, and therefore, a one-dimensional error analysis of the discrete approximation to the viscous terms can give useful insight. In Ref. 4 it was shown that the present scheme is first-order accurate on general stretched meshes, and second-order accuracy is obtained on smoothly stretched meshes. In the present version of the code, the viscous terms have been simplified by taking into account gradients in the direction normal to the viscous shear layers only (thin-layer approximation).

In order to prevent odd–even point decoupling and oscillations near shock waves, and to obtain rapid convergence to the steady state, artificial dissipative terms are added to the governing discrete equations. The artificial dissipation model considered in this paper is based on the work of Jameson, Schmidt, and Turkel.[1] A blend of fourth and second differences is used to provide third-order background dissipation in smooth regions of the flow and first-order dissipation at shock waves, and is given by

$$\boldsymbol{D}_{i,j,k} = (D_\xi^2 - D_\xi^4 + D_\eta^2 - D_\eta^4 + D_\zeta^2 - D_\zeta^4)\boldsymbol{W}_{i,j,k} \tag{9}$$

The second and fourth difference operators read

$$D_\xi^2 \boldsymbol{W}_{i,j,k} = \nabla_\xi [\bar{\lambda}_{\xi i+1/2,j,k} \cdot \varepsilon^{(2)}_{i+1/2,j,k}] \Delta_\xi \boldsymbol{W}_{i,j,k} \tag{10}$$

$$D_\xi^4 \boldsymbol{W}_{i,j,k} = \nabla_\xi [\bar{\lambda}_{\xi i+1/2,j,k} \cdot \varepsilon^{(4)}_{i+1/2,j,k}] \Delta_\xi \nabla_\xi \Delta_\xi \boldsymbol{W}_{i,j,k} \tag{11}$$

where $\Delta_\xi$ and $\nabla_\xi$ are forward and backward difference operators in the $\xi$ direction. In order to avoid excessively large dissipation levels for cells with high aspect ratios and to maintain the good damping properties of the scheme, a variable scaling factor of the dissipative terms is employed, which is an extension of the two-dimensional scheme of Martinelli.[3] The scaling factor is defined as a function of the spectral radii of the Jacobian matrices associated with the $\xi$, $\eta$, and $\zeta$ directions and accounts for varying cell aspect ratios

$$\bar{\lambda}_{\xi i+1/2,j,k} = \lambda_{\xi i+1/2,j,k} \cdot \Phi_{i+1/2,j,k} \tag{12}$$

$$\Phi_{i+1/2,j,k} = 1 + \max\left[\left(\frac{\lambda_{\eta i+1/2,j,k}}{\lambda_{\xi i+1/2,j,k}}\right)^\alpha, \left(\frac{\lambda_{\zeta i+1/2,j,k}}{\lambda_{\xi i+1/2,j,k}}\right)^\alpha\right]$$

$$\lambda_{\xi i+1/2,j,k} = |\boldsymbol{u}_{i+1/2,j,k} \cdot \boldsymbol{S}_{\xi i+1/2,j,k}| + c|\boldsymbol{S}_{\xi i+1/2,j,k}|$$

$$\lambda_{\eta i+1/2,j,k} = |\boldsymbol{u}_{i+1/2,j,k} \cdot \boldsymbol{S}_{\eta i+1/2,j,k}| + c|\boldsymbol{S}_{\eta i+1/2,j,k}|$$

$$\lambda_{\zeta i+1/2,j,k} = |\boldsymbol{u}_{i+1/2,j,k} \cdot \boldsymbol{S}_{\zeta i+1/2,j,k}| + c|\boldsymbol{S}_{\zeta i+1/2,j,k}|$$

where $\boldsymbol{u}_{i+1/2,j,k}$ denotes the velocity vector and $c$ is the speed of sound. The use of the maximum function in the definition of $\Phi$ is important for grids where $\lambda_\eta/\lambda_\xi$ and $\lambda_\zeta/\lambda_\xi$ are very large and of the same order of magnitude. In this case, if these ratios are summed rather than taking the maximum, too large dissipative terms are obtained, which will degrade the solution and may destroy the convergence of the time-stepping scheme. In general, coordinate grids around three-dimensional configurations exhibit larger variations of the cell aspect ratio than two-dimensional grids. Therefore, somewhat less freedom in the choice of the exponent $\alpha$ in three dimensions has been observed. It has been found that the choice $\alpha = 0.5$ yields a robust three-dimensional scheme. The coefficients $\varepsilon^{(2)}$ and $\varepsilon^{(4)}$ use the pressure as a sensor for shocks in the flowfield. They are defined as

$$\varepsilon^{(2)}_{i+1/2,j,k} = k^{(2)} \max(\nu_{i-1,j,k}, \nu_{i,j,k}, \nu_{i+1,j,k}, \nu_{i+2j,k}) \tag{13}$$

$$\nu_{i,j,k} = \left|\frac{p_{i-1,j,k} - 2p_{i,j,k} + p_{i+1,j,k}}{p_{i-1,j,k} + 2p_{i,j,k} + p_{i+1,j,k}}\right|$$

$$\varepsilon^{(4)}_{i+1/2,j,k} = \max\{0, [k^{(4)} - \varepsilon^{(2)}_{i+1/2,j,k}]\}$$

where $k^{(2)}$ and $k^{(4)}$ are constants. The dissipation operators in the $\eta$ and $\zeta$ directions are defined in a similar manner.

## Boundary Conditions

At subsonic inflow/outflow boundaries, a locally one-dimensional flow normal to the boundary is assumed. According to Ref. 11, the governing flow equations are linearized around the values at the end of the previous time step, and the characteristic variables corresponding to outgoing characteristics are extrapolated from the interior. The characteristic variables corresponding to incoming characteristics are determined from the freestream.

At solid walls, the no-slip condition is enforced by setting

$$u = v = w = 0 \tag{14}$$

The continuity and energy equations are solved at the grid points lying on the surface if we assume an adiabatic wall. For the wall points, control volumes are formed by taking the four nearest cells adjacent to the wall. The first derivatives, which are needed at the wall for the evaluation of the viscous terms, are obtained by one-sided difference approximations. Hence, the treatment of the wall points is first-order accurate.

It has been found that the computed velocity distribution near the wall may be significantly affected by the artificial dissipative terms if the stencil of the dissipative terms normal to the wall is not properly defined. The reasons for this are the high grid stretching normal to the wall and the steep velocity gradients of the turbulent boundary layer. When solving the momentum equations at the grid point just outside the wall at $j = 3$, the dissipation operator needs the dependent variables just inside. The extrapolation formula

$$\Delta_\eta \boldsymbol{W}_{i,1,k} = \boldsymbol{W}_{i,2,k} - \boldsymbol{W}_{i,1,k} = 2\Delta_\eta \boldsymbol{W}_{i,2,k} - \Delta_\eta \boldsymbol{W}_{i,3,k} \tag{15}$$

rather than the usual linear form

$$\Delta_\eta \boldsymbol{W}_{i,1,k} = \Delta_\eta \boldsymbol{W}_{i,2,k} \tag{16}$$

results in much less sensitivity of the solution to artificial viscosity and has had no significant drawback on convergence in the computations made so far.

## Turbulence Models

Most of the computations in the present work have been completed using the well-known turbulence model of Baldwin and Lomax.[7] The model is based on algebraic equilibrium expressions for the eddy viscosity in the inner and outer part of the boundary layer.

Frequently, it has been observed that in separated flows, the assumption of equilibrium of the turbulence is not valid. Both convection and diffusion of turbulence have to be taken

into account to allow for a more accurate determination of the turbulent stresses. For this purpose, Johnson and King[8] devised an extended eddy viscosity model for separated wall boundary layers. They postulated that the viscosity of the inner layer near the wall and the shape of the eddy viscosity distribution in the outer layer may be accurately described with algebraic relations if we assume equilibrium. The equilibrium distribution of the outer layer, however, is multiplied with a nonequilibrium factor in such a way that a transport equation for the maximum shear stress in the layer is fulfilled. Thus, the complete model is a nonequilibrium model of turbulence. Here, a slightly modified version of this model is used, which is particularly convenient for use in three-dimensional Navier–Stokes codes. Details of the model and its implementation are given in Ref. 12.

## Time-Stepping Scheme

The system of ordinary differential equations that is obtained by discretization in space is advanced in time with a five-stage Runge–Kutta scheme. A hybrid scheme is used where the artificial dissipative terms are evaluated on the first, third, and fifth stages of the scheme. It has been shown[3] that this scheme has a particularly large parabolic stability limit. For computational efficiency, the physical viscous terms are computed on the first stage and frozen for the remaining stages. Details of the scheme are given in Ref. 4. The steady-state solution is independent of the time step, and therefore, the scheme is amenable to convergence acceleration techniques.

Three methods are employed to accelerate convergence of the basic explicit time-stepping scheme. These techniques are as follows: 1) local time stepping, 2) implicit residual smoothing, and 3) multigrid.

With local time stepping, the solution at each mesh point is advanced at the maximum $\Delta t$ allowed by stability. Both convection and diffusion stability limits are included in the computation of $\Delta t$ (see Ref. 12).

The stability range of the basic time-stepping scheme can be extended using implicit smoothing of the residuals. This technique was first introduced by Lerat[13] for the Lax–Wendroff scheme and later devised by Jameson[14] for the Runge–Kutta scheme. For three-dimensional flows, the residual smoothing can be applied in the form

$$(1-\varepsilon_\xi \nabla_\xi \Delta_\xi)(1-\varepsilon_\eta \nabla_\eta \Delta_\eta)(1-\varepsilon_\zeta \nabla_\zeta \Delta_\zeta)\bar{R}_m = R_m \qquad (17)$$

where the residual $R_m$ is defined by

$$R_m = \alpha_m \frac{\Delta t}{V}(Q_m - D_m), \qquad m = 1,5 \qquad (18)$$

and computed in the Runge–Kutta stage $m$. $Q_m$ is the sum of the convective and diffusive terms, $D_m$ the total artificial dissipation at stage $m$, and $\bar{R}_m$ the final residual at stage $m$ after the sequence of smoothing in the $\xi$, $\eta$, and $\zeta$ directions.

The use of constant coefficients in the implicit treatment has proven to be satisfactory (extending the CFL number by a factor of 2 and 3) even for meshes with cells of high aspect ratio, provided additional support such as enthalpy damping[1] is introduced. However, the use of enthalpy damping, which assumes constant total enthalpy throughout the flowfield, precluded the solution of problems with heat-transfer effects. The need for enthalpy damping can be eliminated by using the variable coefficients $\varepsilon_\xi$, $\varepsilon_\eta$, and $\varepsilon_\zeta$ that account for the variation of the cell aspect ratio.

For this purpose, consider a cell where the edge lengths in the $\xi$ and $\zeta$ directions are much longer than in the $\eta$ direction. The explicit time step is limited by the characteristic wave speed in the direction of the short cell edge. It is obvious that, for an extension of stability, implicit smoothing is required in the $\eta$ direction. If the same implicit residual smoothing is also applied in the other directions, where the characteristic wave speeds are much smaller than the stability limit, the damping behavior of the scheme, which is optimal at wave speeds near the stability limit, is impaired. To overcome this problem, Martinelli[3] has given formulae, which are functions of characteristic wave speeds, for the two-dimensional smoothing coefficients. One extension of Martinelli's form to three dimensions is as follows:

$$\varepsilon_\xi = \max\left(0, \frac{1}{4}\left\{\left[\frac{N}{N^*}\frac{1+\max(r_{\eta\xi}^{\alpha}, r_{\zeta\xi}^{\alpha})}{1+\max(r_{\eta\xi}, r_{\zeta\xi})}\right]^2 - 1\right\}\right) \qquad (19a)$$

$$\varepsilon_\eta = \max\left(0, \frac{1}{4}\left\{\left[\frac{N}{N^*}\frac{1+\max(r_{\eta\xi}^{-\alpha}, r_{\zeta\eta}^{\alpha})}{1+\max(r_{\eta\xi}^{-1}, r_{\zeta\eta})}\right]^2 - 1\right\}\right) \qquad (19b)$$

$$\varepsilon_\zeta = \max\left(0, \frac{1}{4}\left\{\left[\frac{N}{N^*}\frac{1+\max(r_{\zeta\xi}^{-\alpha}, r_{\zeta\eta}^{-\alpha})}{1+\max(r_{\zeta\xi}^{-1}, r_{\zeta\eta}^{-1})}\right]^2 - 1\right\}\right) \qquad (19c)$$

where $N/N^*$ is the ratio of the Courant–Friedrichs–Lewy number of the smoothed scheme to that of the basic explicit scheme; the quantities $r_{\eta\xi}$, $r_{\zeta\xi}$, and $r_{\zeta\eta}$ are defined as

$$r_{\eta\xi} = \frac{\lambda_\eta}{\lambda_\xi}, \qquad r_{\zeta\xi} = \frac{\lambda_\zeta}{\lambda_\xi}, \qquad r_{\zeta\eta} = \frac{\lambda_\zeta}{\lambda_\eta} \qquad (20)$$

and $\lambda_\xi$, $\lambda_\eta$, and $\lambda_\zeta$ are the characteristic speeds defined in (12); the range of the exponent is $0 < \alpha < 1$, and typically $\alpha = 0.5$. Note that throughout this section the subscripts $\xi$, $\eta$, and $\zeta$ refer to coordinate directions. For a stability analysis of this set of smoothing coefficients, we consider the scalar hyperbolic equation

$$\frac{\partial w}{\partial t} + a\frac{\partial w}{\partial x} + b\frac{\partial w}{\partial y} + c\frac{\partial w}{\partial z} = 0 \qquad (21)$$

which describes three-dimensional wave propagation. Using central-difference approximations for the spatial derivatives, we can write a semidiscrete form for (21) as

$$\begin{aligned}\Delta t \frac{\mathrm{d}w}{\mathrm{d}t} = &-\frac{N_\xi}{2}(w^n_{i+1,j,k} - w^n_{i-1,j,k}) \\ &-\frac{N_\eta}{2}(w^n_{i,j+1,k} - w^n_{i,j-1,k}) \\ &-\frac{N_\zeta}{2}(w^n_{i,j,k+1} - w^n_{i,j,k+1})\end{aligned} \qquad (22)$$

where the Courant numbers

$$N_\xi = \lambda_\xi \frac{\Delta t}{V}, \qquad N_\eta = \lambda_\eta \frac{\Delta t}{V}, \qquad N_\zeta = \lambda_\zeta \frac{\Delta t}{V} \qquad (23)$$

and

$$\lambda_\xi = a\,\Delta y\,\Delta z, \qquad \lambda_\eta = b\,\Delta x\,\Delta z, \qquad \lambda_\zeta = c\,\Delta x\,\Delta y \qquad (24)$$

If we take the Fourier transform of (22), the following is obtained:

$$\Delta t \frac{\mathrm{d}\hat{w}}{\mathrm{d}t} = -i(N_\xi \sin\Theta_\xi + N_\eta \sin\Theta_\eta + N_\zeta \sin\Theta_\zeta)\hat{w}^n \qquad (25)$$

where the caret indicates a transformed quantity, and $\Theta_\xi$, $\Theta_\eta$, and $\Theta_\zeta$ are the Fourier angles for each coordinate direction. If implicit residual smoothing is applied, then (25) is replaced with

$$\Delta t \frac{\mathrm{d}\hat{w}}{\mathrm{d}t} = Z\hat{w}^n \qquad (26)$$

and the Fourier symbol

$$Z = \frac{-i(N_\xi \sin\Theta_\xi + N_\eta \sin\Theta_\eta + N_\zeta \sin\Theta_\zeta)}{\beta_\xi \beta_\eta \beta_\zeta} \tag{27}$$

where

$$\begin{aligned} \beta_\xi &= 1 + 2\varepsilon_\xi(1 - \cos\Theta_\xi) \\ \beta_\eta &= 1 + 2\varepsilon_\eta(1 - \cos\Theta_\eta) \\ \beta_\zeta &= 1 + 2\varepsilon_\zeta(1 - \cos\Theta_\zeta) \end{aligned} \tag{28}$$

A sufficient condition for stability is

$$|Z| \le N^* \quad \text{for all} \quad \Theta_\xi, \Theta_\eta, \Theta_\zeta \tag{29}$$

and $N^*$ is the Courant number of the unsmoothed scheme. Let

$$F = F(\Theta_\xi, \Theta_\eta, \Theta_\zeta) = \frac{|Z|}{N^*} \tag{30}$$

and

$$\begin{aligned} \bar{F} &= \bar{F}(\Theta_\xi, \Theta_\eta, \Theta_\zeta) \\ &= \frac{N_\xi}{N^*} f(\Theta_\xi) + \frac{N_\eta}{N^*} g(\Theta_\eta) + \frac{N_\zeta}{N^*} h(\Theta_\zeta) \end{aligned} \tag{31}$$

where

$$f(\Theta_\xi) = \frac{\sin\Theta_\xi}{\beta_\xi}, \qquad g(\Theta_\eta) = \frac{\sin\Theta_\eta}{\beta_\eta}, \qquad h(\Theta_\zeta) = \frac{\sin\Theta_\zeta}{\beta_\zeta}$$

Clearly,

$$F \le \bar{F} \tag{32}$$

and the maximum of $F$

$$F_{\max} \le \bar{F}_{\max} = \frac{N_\xi}{N^*} f_{\max} + \frac{N_\eta}{N^*} g_{\max} + \frac{N_\zeta}{N^*} h_{\max} \tag{33}$$

By differentiating the functions $f$, $g$, and $h$ with respect to $\Theta_\xi$, $\Theta_\eta$, and $\Theta_\zeta$, respectively, and determining where the derivatives vanish, we find that

$$f_{\max} = \frac{1}{\sqrt{1 + 4\varepsilon_\xi}} \tag{34a}$$

$$g_{\max} = \frac{1}{\sqrt{1 + 4\varepsilon_\eta}} \tag{34b}$$

$$h_{\max} = \frac{1}{\sqrt{1 + 4\varepsilon_\zeta}} \tag{34c}$$

Thus,

$$\bar{F}_{\max} = \frac{N_\xi}{N^*} \frac{1}{\sqrt{1 + 4\varepsilon_\xi}} + \frac{N_\eta}{N^*} \frac{1}{\sqrt{1 + 4\varepsilon_\eta}} + \frac{N_\zeta}{N^*} \frac{1}{\sqrt{1 + 4\varepsilon_\zeta}} \tag{35}$$

If

$$\Delta t = N \frac{V}{\lambda_\xi + \lambda_\eta + \lambda_\zeta} \tag{36}$$

and $N_\xi$, $N_\eta$, and $N_\zeta$ of (23) are substituted into (35),

$$\begin{aligned} \bar{F}_{\max} = &\frac{N}{N^*} \frac{1}{1 + r_{\eta\xi} + r_{\zeta\xi}} \frac{1}{\sqrt{1 + 4\varepsilon_\xi}} \\ &+ \frac{N}{N^*} \frac{1}{1 + r_{\eta\xi}^{-1} + r_{\zeta\eta}} \frac{1}{\sqrt{1 + 4\varepsilon_\eta}} \\ &+ \frac{N}{N^*} \frac{1}{1 + r_{\zeta\xi}^{-1} + r_{\zeta\eta}^{-1}} \frac{1}{\sqrt{1 + 4\varepsilon_\zeta}} \end{aligned} \tag{37}$$

So we need only to demonstrate that $\bar{F}_{\max} \le 1$ in order to satisfy the sufficient condition of (29) for stability. Suppose that for simplicity, we take $a = b = c = 1$ in the model problem. Then, the characteristic speed ratios of (20) can be written as

$$r_{\eta\xi} = \frac{\Delta x}{\Delta y}, \qquad r_{\zeta\xi} = \frac{\Delta x}{\Delta z}, \qquad r_{\zeta\eta} = \frac{\Delta y}{\Delta z} \tag{38}$$

Consider the case of large cell aspect ratio (AR) and let $r_{\eta\xi} \gg 1$, $r_{\zeta\xi} = 1$ (i.e., meshes appropriate for solving the thin-layer Navier–Stokes equations). Then, the residual smoothing coefficients of (19) behave as

$$\varepsilon_\xi \to 0 \tag{39a}$$

$$\varepsilon_\eta \to \frac{1}{4}\left[\left(\frac{N}{N^*} \frac{1 + r_{\zeta\eta}^\alpha}{1 + r_{\zeta\eta}}\right)^2 - 1\right] \tag{39b}$$

$$\varepsilon_\zeta \to 0 \tag{39c}$$

which is a one-dimensional smoothing. Substituting these coefficients into $\bar{F}_{\max}$ of (37), we obtain

$$\bar{F}_{\max} \approx \frac{1}{1 + r_{\zeta\eta}^\alpha} < 1 \tag{40}$$

and the sufficiency condition is satisfied. If $r_{\eta\xi} \gg 1$ and $r_{\zeta\xi} \gg 1$ (i.e., both $\Delta y$ and $\Delta z$ are small, which is the case for meshes used for computing viscous flows over solid-surface juncture regions), we get

$$\varepsilon_\xi \to 0 \tag{41a}$$

$$\varepsilon_\eta \to \frac{1}{4}\left[\left(\frac{N}{N^*} \frac{1 + r_{\zeta\eta}^\alpha}{1 + r_{\zeta\eta}}\right)^2 - 1\right] \tag{41b}$$

$$\varepsilon_\zeta \to \frac{1}{4}\left[\left(\frac{N}{N^*} \frac{1 + r_{\zeta\eta}^{-\alpha}}{1 + r_{\zeta\eta}^{-1}}\right)^2 - 1\right] \tag{41c}$$

which is a two-dimensional smoothing. In this case,

$$\bar{F}_{\max} \approx \frac{1}{1 + r_{\zeta\eta}^\alpha} + \frac{1}{1 + r_{\zeta\eta}^{-\alpha}} = 1 \tag{42}$$

and the stability condition is satisfied. One can also show easily that the stability condition is satisfied for the corresponding cases for small AR and for the case of AR = 1.0 ($\Delta x = \Delta y = \Delta z$). In order to determine that stability is achieved for a full range of cell aspect ratios and Courant numbers, a numerical investigation was performed. The stability behavior of the five-stage Runge–Kutta scheme with implicit residual smoothing was studied for the model problem by systematically varying $\Theta_\xi$, $\Theta_\eta$, and $\Theta_\zeta$ between 0 and $2\pi$ and taking $\Delta\Theta_\xi = \Delta\Theta_\eta = \Delta\Theta_\zeta = 2\pi/40$. The maximum modulus of the Fourier symbol $Z$ was computed for cell aspect ratios in the range of $10^{-3}$ to $10^3$ and Courant number ratios $N/N^*$ varying from 1 to $10^3$. The following two cases were examined for each specified Courant number: 1) the ratio $r_{\eta\xi} = \Delta x/\Delta y$ was varied and $r_{\zeta\xi} = \Delta x/\Delta z = 1$; and 2) the ratios $r_{\eta\xi}$ and $r_{\zeta\xi}$ were varied. In all cases, the stability condition of (29), where $N^* = 4$ for the five-stage scheme, was

satisfied. These results and the analysis suggest that the five-stage scheme considered here in conjunction with implicit residual smoothing based on the coefficients of (19) is unconditionally stable (in the linear sense).

Some additional comments concerning the stability of the five-stage scheme with implicit residual smoothing are appropriate. If standard third-order dissipation terms are introduced into the model problem of (21), the unconditional stability behavior is maintained. However, as the Courant number becomes large, the contribution of the dissipation terms to the Fourier symbol goes to zero; and consequently, the high frequencies are undamped. Thus, the practical limit for the Courant number is determined principally by the requirement for good high-frequency damping characteristics, which allows the construction of an effective driving scheme for a multigrid method. Typically, values around 2 are used for $N/N^*$.

Finally, a multigrid method is employed that is based on the work of Jameson.[2] For the multigrid process, coarser meshes are obtained by eliminating every other mesh line in each coordinate direction. The solution is transferred to coarser meshes by injection. Residuals are transferred from fine to coarse meshes by a weighted average over the fine-mesh grid points that are nearest to the point on the coarse mesh. A forcing function is constructed so that the solution on a coarse mesh is driven by the residuals collected on the next finer mesh. This procedure is repeated on each succeeding coarser mesh until the coarsest mesh is reached. Then, the corrections are transferred to the next finer mesh by trilinear interpolation. A fixed W-type cycle is used to execute the multigrid strategy. The robustness of the multigrid scheme is greatly improved by smoothing the total corrections before the solution is updated. That is,

$$\boldsymbol{W}^{(n+1)} = \boldsymbol{W}^n + \Delta \boldsymbol{W}_{\text{tot}} \tag{43}$$

where

$$\Delta \boldsymbol{W}_{\text{tot}} = \Delta \boldsymbol{W}_F + \Delta \boldsymbol{W}_C$$

The quantity $\Delta \boldsymbol{W}_F$ is the solution correction from the finest grid, and $\Delta \boldsymbol{W}_C$ is the resultant solution correction from the coarse grids. The smoothing reduces high-frequency oscillations introduced by the linear interpolation of the coarse mesh corrections, and hence, convergence of the scheme is obtained for a much broader range of dissipation coefficients. The factored scheme of (17) with constant coefficients ($\varepsilon_\xi = \varepsilon_\eta = \varepsilon_\zeta = 0.2$) is used for this smoothing. Additional robustness of the multigrid scheme is achieved by computing more than a single time step on the coarse meshes. The use of multiple time steps on the coarse meshes improves the damping characteristics on the coarse meshes. Thus, smaller values of coarse-mesh dissipation may be used, which results in an improvement of the convergence to the steady state. Finally, the application of a full multigrid method provides a well-conditioned starting solution for the finest mesh being considered.

## Results

Before examining the accuracy and convergence behavior of the three-dimensional scheme, it is appropriate to look at the results of a simplified version of the code for two-dimensional flows. There are several reasons for this. First, as already mentioned, two-dimensional grids around airfoils

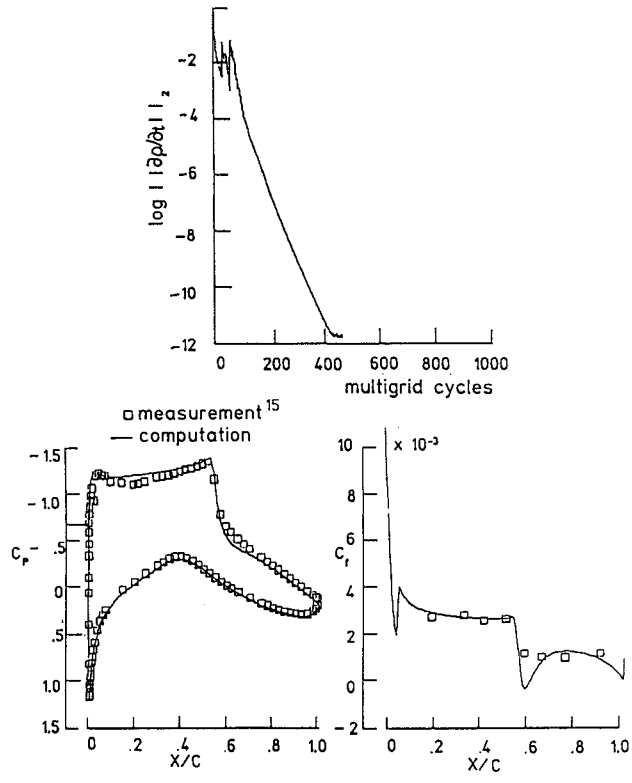


**Fig. 3 Convergence history and distributions of pressure and skin friction for flow around RAE 2822 airfoil, $M_\infty = 0.73$, $\alpha = 2.79$ deg, $Re_\infty = 6.5 \times 10^6$, grid $321 \times 65$, $k^{(4)} = 1/32$, and $k^{(2)} = 1/2$.**

**Table 1 Convergence behavior for two- and three-dimensional flows. Numbers denote the multigrid cycles on the fine mesh required to obtain the convergence criterion. Numbers in parentheses are the total computation times in seconds on the CRAY-2. Dissipation coefficients $k^{(4)} = 1/32$ and $k^{(2)} = 1/2$.**

| Case | Grid | Turbulence model | No. time steps on coarse mesh | 1% $C_L$ | 0.1% $C_L$ | S.S. Pts. | $10^{-5}$ Red. | $C_L$ | $C_D$ |
|---|---|---|---|---|---|---|---|---|---|
| RAE 2822 $M_\infty = 0.73$ $\alpha = 2.79$ deg $Re = 6.5 \times 10^6$ | $321 \times 65$ | B.-L. | 2 | 14(32.9) | 31(55.5) | 41(68.9) | 130(187.2) | 0.8346 | 0.01727 |
| ONERA-M6 $M_\infty = 0.84$ $\alpha = 3.06$ deg $Re_\infty = 11 \times 10^6$ | $289 \times 65 \times 49$ | B.-L. | 1 | 6(886) | 54(3745) | 167(10412) | 460(27580) | 0.2677 | 0.01782 |
| | $289 \times 65 \times 49$ | B.-L. | 2 | 4(810) | 38(3204) | 138(10244) | — | 0.2677 | 0.01782 |
| ONERA-M6 $M_\infty = 0.84$ $\alpha = 6.06$ deg $Re_\infty = 11 \times 10^6$ | $289 \times 65 \times 49$ | B.-L. | 1 | 21(2012) | 44(3362) | — | — | 0.5380 | 0.05559 |
| | $289 \times 65 \times 49$ | J.-K. | 1 | 74(4944) | 135(8482) | — | — | 0.5085 | 0.05394 |
| | $289 \times 65 \times 49$ | J.-K. | 2 | 44(3638) | 79(6102) | — | — | 0.5085 | 0.05394 |

generally exhibit less variation of the cell aspect ratio than grids around finite-span wings. Second, three-dimensional grids around the wing tip usually show considerable skewness, which can slow down convergence. Finally, the three-dimensional flow around the wing usually separates at the wing tip, thereby forming a vortex sheet. The presence of the vortex sheet can lead to unphysical values of the turbulent viscosity in this region, which in turn may slow down or prohibit the convergence of the time-stepping scheme.

In order to demonstrate the capabilities of the present method, the transonic flow around the RAE 2822 airfoil is considered. A coordinate grid of $321 \times 65$ points with 256 points on the airfoil surface is used for the computation. The distance to the first grid point away from the wall is $10^{-5}$ chords. A typical value of $y^+$ at the first grid point away from the wall is 2 for this flow case. The resulting skin friction distribution is not very sensitive to this choice, i.e., the skin friction drag changes from 0.005446 to 0.005205 when doubling the first grid spacing and to 0.005408 with half the value. A detailed investigation of the effect of grid density on the accuracy of the two-dimensional code has been presented in Ref. 4. In the multigrid process, two time steps are executed on each of the coarse meshes. The convergence behavior and distributions of pressure and skin friction for $M_\infty = 0.73$, $\alpha = 2.79$ deg, and $Re_\infty = 6.5 \times 10^6$ are shown in Fig. 3. An error reduction of 10 orders of magnitude is obtained within 340 cycles on the fine mesh. The lift coefficient converges to 0.1% within the final value in 31 cycles on the fine mesh, the pressure drag in 32 cycles, and the skin friction drag in 19 cycles. By using additional convergence criteria as given in Table 1, it is shown that engineering accuracy is obtained within 40 multigrid cycles on the finest mesh.

Next, the transonic flow over the ONERA-M6 wing is considered. A computational mesh with a C-type topology in the streamwise direction and an O-type topology in the spanwise direction and $289 \times 65 \times 49$ points is used. The distance to the first grid point away from the wall is $10^{-5}$ local chord lengths, which corresponds to typical $y^+$ values of 3. There is considerable skewness in the wing-tip region, as shown in Fig. 4. A somewhat coarser mesh also has been used with $193 \times 49 \times 33$ points. Figure 5 shows the convergence behavior of the three-dimensional scheme for $M_\infty = 0.84$ and $Re_\infty = 11 \times 10^6$. Two flow cases, namely, $\alpha = 3.06$ deg with attached flow and $\alpha = 6.06$ deg with a strong separation on the upper surface, are considered. For the attached-flow case, the influence of the fourth-difference dissipation on convergence is displayed in Fig. 5a. The coefficient of the second-difference dissipation $k^{(2)} = 1/2$ has been kept unchanged in all computations. The convergence is not as good as for the two-dimensional cases. The largest residuals occur at the wing tip, where the grid is highly skewed. In order to investigate the effects of grid skewness on the convergence, additional runs of the code have been made using improved meshes, but the convergence rates were hardly changed on these meshes.

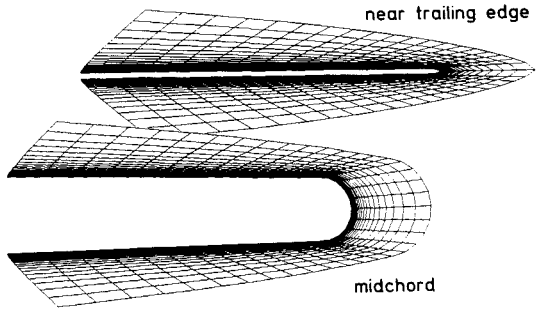


Fig. 4 Spanwise sections of mesh around ONERA-M6 wing.

The decrease of residuals vs multigrid cycles is not much affected by multiple time stepping on the coarse meshes (not shown here). Apparently, there are high-frequency oscillations on the fine mesh, which are only slowly damped, and this behavior is not improved using more work on the coarse meshes. The convergence of the global flowfield, however, is improved as shown in Table 1. The improvements that are obtained by multiple time stepping on the coarse meshes are more pronounced for the separated flow case as shown in Fig. 5b. Here, the interaction process between the shock and separating boundary layers is considerably accelerated, and converged values of lift and drag are obtained more rapidly (see Table 1). From Table 1, it is evident that the solution of the separated-flow case converges more rapidly with the Baldwin–Lomax turbulence model than with the Johnson–King model. This is due to the much larger size of the flow separation with the Johnson–King model and a strong shock boundary-layer interaction; see subsequent sections. The computational penalty of the Johnson–King model per multigrid cycle, however, is negligible. The dashed lines in Table 1 with respect to the convergence of the number of supersonic points for the separated-flow case indicate that about 250 multigrid cycles were not sufficient for this criterion. However, the final convergence rate of the residuals for the separated-flow case is quite comparable to that for the attached-flow case. Hence, an eventually converged solution can be expected for both flow cases.

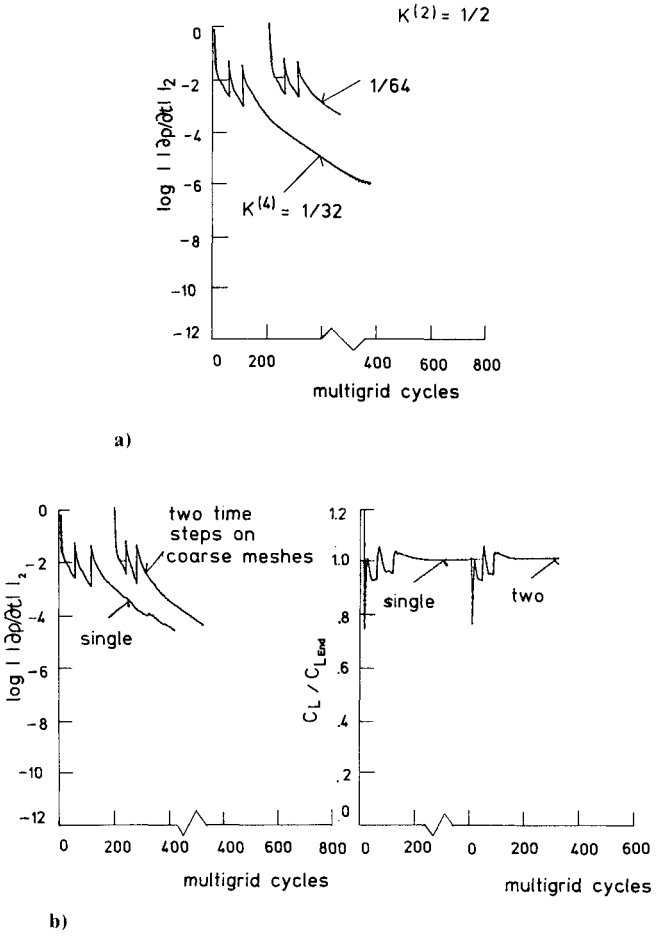


Fig. 5 Convergence behavior for transonic flow around ONERA-M6 wing, $M_\infty = 0.84$, $Re_\infty = 11.0 \times 10^6$, mesh $289 \times 65 \times 49$. a) Influence of fourth-difference dissipation on convergence, single time step on coarse meshes, $\alpha = 3.06$ deg, Baldwin–Lomax model. b) Convergence for nonequilibrium Johnson–King turbulence model, $k^{(4)} = 1/32$, $\alpha = 6.06$ deg.

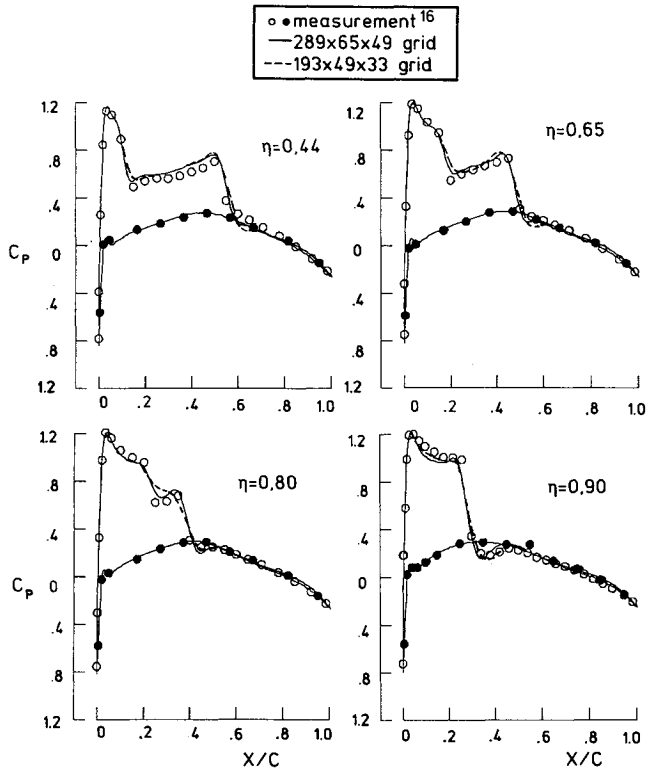


**Fig. 6 Pressure distribution for ONERA-M6 wing, $M_\infty = 0.84$, $\alpha = 3.06$ deg, $Re_\infty = 11.0 \times 10^6$, $k^{(4)} = 1/32$, computed with the Baldwin–Lomax model.**

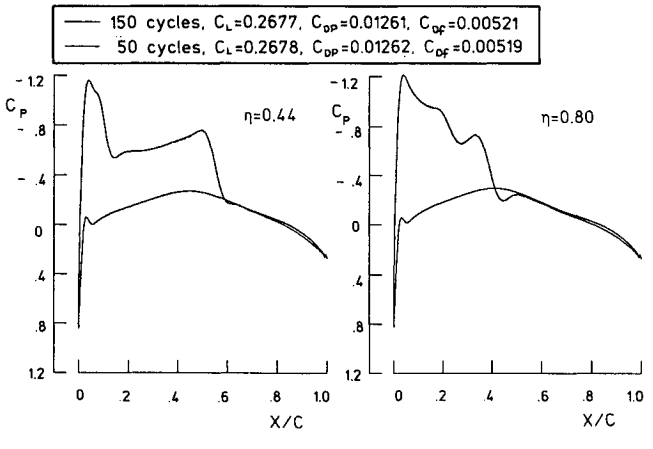


**Fig. 7 Comparison of pressure distribution on ONERA-M6 wing, $M_\infty = 0.84$, $\alpha = 3.06$ deg, $Re_\infty = 11.0 \times 10^6$, $k^{(4)} = 1/32$, Baldwin–Lomax model, after 50 multigrid cycles with the fully converged result, two time steps on the coarse meshes.**

The pressure distributions along several spanwise stations of the wing are displayed for the attached-flow case in Fig. 6. The results of the $289 \times 65 \times 49$ mesh agree well with those from the coarser mesh and with experimental data.[16] From Table 1, it is evident that the global features of the flow converge rapidly. Indeed, plots of the solution after 50 multigrid cycles and the values of lift, pressure drag, and friction drag, which are displayed in Fig. 7, show virtually no differences to the fully converged solution. The effect of reducing the coefficient of the fourth-difference dissipation from 1/32 to 1/64 (not shown here) is to slightly improve shock resolution.

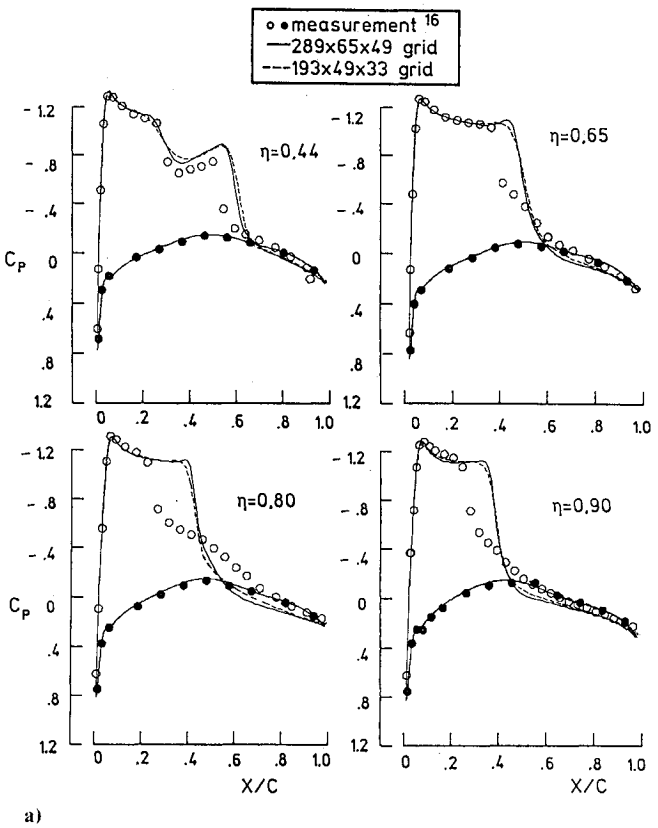


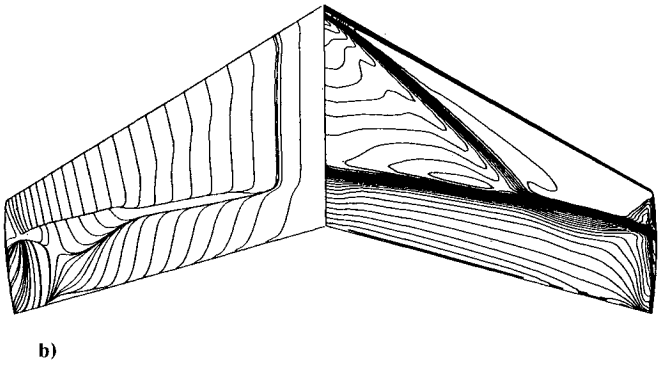


**Fig. 8 Results for ONERA-M6 wing, $M_\infty = 0.84$, $\alpha = 6.06$ deg, $Re_\infty = 11.0 \times 10^6$, $k^{(4)} = 1/32$, computed with the Baldwin–Lomax model. a) Pressure distributions in four wing sections. b) Wall streamlines and isobars on the upper wing surface.**

The total force coefficients for $k^{(4)} = 1/64$ are $C_L = 0.2704$ and $C_D = 0.01782$.

Results for the separated-flow case are displayed in Fig. 8. With the Baldwin–Lomax turbulence model, large discrepancies between computation and experiment occur. The size of the separated region is underpredicted, and consequently, the shock is located too far downstream. The agreement between computation and experimental data is greatly improved with the Johnson–King model, Fig. 9. The size of the separated region and location of the shock compare well with the data. The wall streamlines show a mushroom-type structure that is typical for wings at a high angle of attack. Table 1 shows that approximately 80 multigrid cycles on the fine mesh are sufficient for convergence to engineering accuracy. If the $193 \times 49 \times 33$ grid is considered to be sufficiently fine, 80 multigrid cycles require less than 40 min CPU time on the CRAY-2 computer.

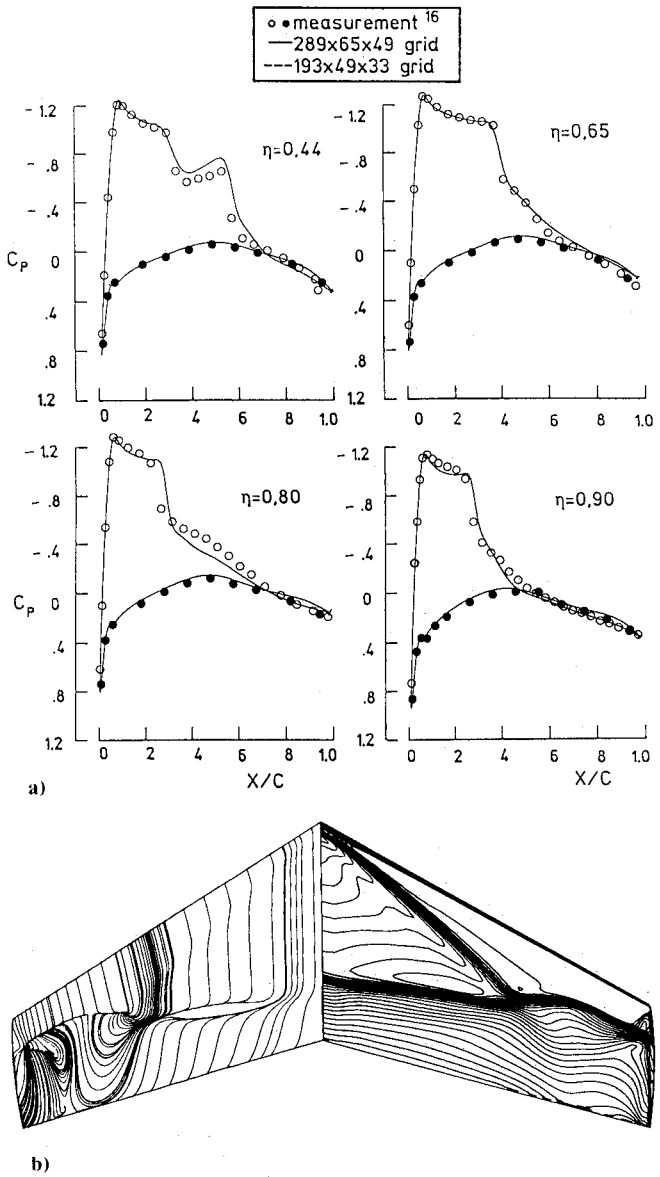


**Fig. 9 Results for ONERA-M6 wing, $Ma_\infty = 0.84$, $\alpha = 6.06$ deg, $Re_\infty = 11.0 \times 10^6$, $k^{(4)} = 1/32$, computed with the Johnson–King model. a) Pressure distributions in four wing sections. b) Wall streamlines and isobars on the upper wing surface.**

## Concluding Remarks

A cell-vertex scheme for the Navier–Stokes equations, which is based on central-difference approximations and Runge–Kutta time stepping, has been described. By using local time stepping, implicit residual smoothing with locally varying coefficients, a multigrid method, and carefully controlled artificial dissipative terms, very good convergence rates are obtained for two- and three-dimensional flows. Details of the acceleration techniques, which are important for convergence on meshes with high-aspect-ratio cells, have been discussed. In particular, the stability properties of the implicit smoothing of the explicit residuals with coefficients, which depend on cell aspect ratios, have been analyzed. In general, engineering accuracy is obtained within 40 multigrid cycles on the fine mesh for two-dimensional flows, and within 50 to 80 multigrid cycles in three dimensions. The accuracy of the code is examined by grid refinement studies and comparison with experimental data. The results for attached- and separated-flow cases show that the present code can be considered a useful tool in the design of transonic wings.

## Acknowledgments

The present work evolved as a result of a scientific exchange program between DLR and NASA, while the first author was at the NASA Langley Research Center. The authors are indebted to Dr. R. Abid for sharing his knowledge about the Johnson–King turbulence model, and to B. W. Wedan for generating the three-dimensional grids.

## References

[1]Jameson, A., Schmidt, W., and Turkel, E., "Numerical Solutions of the Euler Equations by Finite Volume Methods Using Runge–Kutta Time-Stepping Schemes," AIAA Paper 81-1259, June 1981.

[2]Jameson, A., "Multigrid Algorithms for Compressible Flow Calculations," Mechanical and Aerospace Engineering Rept. 1743, Princeton Univ., NJ, text of lecture given at 2nd European Conference on Multigrid Methods, Cologne, FRG, Oct. 1985.

[3]Martinelli, L., "Calculations of Viscous Flows with a Multigrid Method," Ph.D. dissertation, MAE Dept., Princeton Univ., NJ, 1987.

[4]Radespiel, R., and Swanson, R. C., "An Investigation of Cell Centered and Cell Vertex Multigrid Schemes for the Navier–Stokes Equations," AIAA Paper 89-0548, Jan. 1989.

[5]Jayaram, M., and Jameson, A., "Multigrid Solution of the Navier–Stokes Equations for Flows over Wings," AIAA Paper 88-0705, Jan. 1988.

[6]Rossow, C. C., Kroll, N., Radespiel, R., and Scherr, S., "Investigation of the Accuracy of Finite Volume Methods for 2- and 3-Dimensional Flows," AGARD-CP-437, Vol. 2. 1988, p. 14.

[7]Baldwin, B. S., and Lomax, H., "Thin Layer Approximation and Algebraic Model for Separated Turbulent Flows," AIAA Paper 78-257, Jan. 1978.

[8]Johnson, D. A., and King, L. S., "A New Turbulence Closure Model for Boundary Layer Flows with Strong Adverse Pressure Gradients and Separation," AIAA Paper 84-0175, Jan. 1984.

[9]Jameson, A., "A Vertex Based Multigrid Algorithm for Three-Dimensional Compressible Flow Calculations," in *Numerical Methods for Compressible Flows—Finite Differences, Element and Volume Techniques*, edited by T. E. Tezduar and T. J. R. Hughes, Applied Mechanics Division 78, ASME, New York, 1986, pp. 45–73.

[10]Rossow, C.-C., "Berechnung von Strömungsfeldern durch Lösung der Euler-Gleichungen mit einer erweiterten Finite-Volumen Diskretisierungsmethode," dissertation, TU Braunschweig, 1989.

[11]Whitfield, D. L., and Janus, J. M., "Three-Dimensional Unsteady Euler Equations Solution Using Flux Vector Splitting," AIAA Paper 84-1552, June 1984.

[12]Radespiel, R., "A Cell-Vertex Multigrid Method for the Navier–Stokes Equations, "NASA-TM 101557, 1989.

[13]Lerat, A., "Une classe de schemas aux differences implicites pour les systemes hyperboliques de lois de conservation," *Comptes Rendus Academie Sciences Paris*, Vol. 288A, June 1979, pp. 1033–1036.

[14]Jameson, A., "The Evolution of Computational Methods in Aerodynamics," *Journal of Applied Mechanics*, Vol. 50, Dec. 1983, pp. 1052–1070.

[15]Cook, P. H., McDonald, M. A., and Firmin, M. C. P., "Aerofoil RAE 2822—Pressure Distributions and Boundary Layer and Wake Measurements," AGARD-AR-138, 1979.

[16]Schmitt, V., and Charpin, F., "Pressure Distributions on the ONERA-M6-Wing at Transonic Mach Numbers," AGARD-AR-138, 1979.